Mathematical and Computational Applications

MDPI

Article

Morlet Cross-Wavelet Analysis of Climatic State Variables Expressed as a Function of Latitude, Longitude, and Time: New Light on Extreme Events

Jean-Louis Pinault

Independent Researcher, 96, Rue du Port David, 45370 Dry, France; jeanlouis_pinault@hotmail.fr

Abstract: This study aims to advance our knowledge in the genesis of extreme climatic events with the dual aim of improving forecasting methods while clarifying the role played by anthropogenic warming. Wavelet analysis is used to highlight the role of coherent Sea Surface Temperature (SST) anomalies produced from short-period oceanic Rossby waves resonantly forced, with two case studies: a Marine Heatwave (MHW) that occurred in the northwestern Pacific with a strong climatic impact in Japan, and an extreme flood event that occurred in Germany. Ocean–atmosphere interactions are evidenced by decomposing state variables into period bands within the cross-wavelet power spectra, namely SST, Sea Surface Height (SSH), and the zonal and meridional modulated geostrophic currents as well as precipitation height, i.e., the thickness of the layer of water produced during a day, with regard to subtropical cyclones. The bands are chosen according to the different harmonic modes of the oceanic Rossby waves. In each period band, the joint analysis of the amplitude and the phase of the state variables allow the estimation of the regionalized intensity of anomalies versus their time lag in relation to the date of occurrence of the extreme event. Regarding MHWs in the northwestern Pacific, it is shown how a warm SST anomaly associated with the northward component of the wind resulting from the low-pression system induces an SST response to latent and sensible heat transfer where the latitudinal SST gradient is steep. The SST anomaly is then shifted to the north as the phase becomes homogenized. As for subtropical cyclones, extreme events are the culmination of exceptional circumstances, some of which are foreseeable due to their relatively long maturation time. This is particularly the case of ocean–atmosphere interactions leading to the homogenization of the phase of SST anomalies that can potentially contribute to the supply of low-pressure systems. The same goes for the coalescence of distinct low-pressure systems during cyclogenesis. Some avenues are developed with the aim of better understanding how anthropogenic warming can modify certain key mechanisms in the evolution of those dynamic systems leading to extreme events.

Keywords: wavelet analysis; extreme subtropical cyclones; climate change; sea surface temperature anomalies; oceanic Rossby waves; Marine Heatwaves

Citation: Pinault, J.-L. Morlet Cross-Wavelet Analysis of Climatic State Variables Expressed as a Function of Latitude, Longitude, and Time: New Light on Extreme Events. *Math. Comput. Appl.* **2022**, *27*, 50. https://doi.org/10.3390/mca27030050

Academic Editor: Leonardo Trujillo

Received: 28 April 2022
Accepted: 2 June 2022
Published: 4 June 2022

1. Introduction

Although they seem distant, Marine Heatwaves (MHWs) and extreme subtropical cyclones have a common origin, the resonant forcing of oceanic Rossby waves at mid-latitudes. The present research is focused on those Rossby waves whose period varies from a few days to a few months. At mid-latitudes, they form preferentially where the western boundary currents move away from the continents to re-enter the subtropical gyres [1]. These Rossby waves induce very active convergent or divergent geostrophic currents in the formation of positive or negative Sea Surface Temperature (SST) anomalies. They appear as harmonics of an annual fundamental Rossby wave resonantly forced by the declination of the sun.

While the climatic impact of Rossby waves is well known, their interaction with the atmosphere still presents some mysteries. However, behind this natural cause, there

is a reality: these extreme events are becoming more and more frequent, as numerous studies show. There is therefore a compelling need to elucidate how anthropogenic warming intervenes in the genesis of these extreme events in order to better understand the ocean–atmosphere interactions involved as well as to better anticipate them.

The proposed method consists in representing, in contiguous bands of periods, the amplitude and the time lag, with respect to the date of occurrence of the extreme event, of each of the climatic state variables. For this, both the amplitude and the phase of the climatic state variables are mapped. The amplitude and the phase are deduced from the cross-wavelet power spectra of these state variables expressed as a function of longitude and latitude, and from a reference time series representative of the evolution of the extreme event. In order to optimize the temporal resolution of the dynamics of the observed phenomena, the cross-wavelet power spectra are both scale-averaged over the bandwidths and time-averaged over a time interval bracketing the date of occurrence of the extreme event, the length of which is equal to the bandwidth.

1.1. Marine Heatwaves

MHWs are observed in all oceans. They have impacted fishery resources and the occurrence of harmful algal blooms where rich marine ecosystems are at risk [2]. For example, recent MHW events in the Tasman Sea have had dramatic impacts on the ecosystems, fisheries, and aquaculture off Tasmania's east coast [3]. Similar damages have been investigated in the South China Sea where MHWs were strongly regulated by El Niño–Southern Oscillation (ENSO) [4]. The high latitudes are not spared: Alaska was impacted in 2016 [5]. The economic impact of these events, little known until the recent past, has given rise to much research in recent years. However, our understanding of the large-scale drivers and potential predictability of MHW events is still in its infancy.

The dynamic processes related to the initiation of an advective MHW were investigated in continental shelves, namely the Middle Atlantic Bight of the Northwest Atlantic [6], the North West Australia [7], the Indonesian-Australian Basin and areas including the Timor Sea and Kimberley shelf [8], and in the Pacific shelf waters off southeast Hokkaido, Japan [9]. Favorable climatic conditions are mentioned for driving cross-isobath intrusions of warm, salty offshore water onto the continental shelf.

Long-term temperature changes under the influence of human-induced greenhouse gas-forcing drive coastal MHW trends globally. Cross-shore gradients of MHW and SST changes are reported in the Chilean coast region [10], in mid-latitude coasts like the Mediterranean Sea, Japan Sea, and Tasman Sea, as well as in the northeastern coast of the United States [11], along the Australian coastlines [12], in the Tasman Sea [13], in Canada's British Columbia coastal waters, from Queen Charlotte Strait to the Strait of Georgia [14], in the Coastal Zone of Northern Baja California [15], in the Southern California Bight [16], and in the Oyashio region [17–22].

Studies focused on MHWs have reported conditions favoring the warming of surface waters caused by increased solar radiation because of reduced cloud cover, namely in summer MHWs in the South China Sea [18], in the East China Sea, and the South Yellow Sea [19]. The genesis and trend of MHWs in the Indian Ocean and their role in modulating the Indian summer monsoon have been investigated [20], as well as the role of oceanic Rossby waves forced in the interior South Pacific on observed MHW occurrences off southeast Australia [3].

Finally, intense MHWs occurred at the sea surface over extensive areas of the northwestern Pacific Ocean, including the entire Sea of Japan and part of the Sea of Okhotsk [21,22]. An extreme event due to its extension and intensity, occurred in July–August 2021 [21]. In this article, we will attempt to highlight the role played by oceanic Rossby waves in the genesis of this event, the conditions of formation of which have not yet been fully elucidated.

1.2. Extreme Subtropical Cyclones

The intensity of the heaviest extreme precipitation events is known to increase with global warming [23–27] almost everywhere in the world [28,29]. Particularly impacted are regions subject to subtropical cyclones [30]. At mid-latitudes, these regions are easily identifiable by their precipitation pattern in the 5–10 year band, while they only show a weak seasonality [31,32]. The main areas subject to rainfall oscillation in the 5–10 year band are: (a) Southwest North America, (b) Texas, (c) Southeastern North America, (d) Northeastern North America, (e) Southern Greenland, (f) Europe and Central and Western Asia, (g) the region of the Río de la Plata, (h) Southwestern and Southeastern Australia, and (i) Southeast Asia.

Global warming is projected to lead to a higher intensity of precipitation and longer dry periods in North America [33–35] and Europe [36–41]. Extreme floods during the recent decades in Europe are more frequent compared to the last 500 years [42]. For Germany, the number of people exposed to flood risks could more than triple and damages more than quadruple by the end of the century [43,44]. In summer, an increase is also projected in most parts of Europe, although decreases are projected for some regions in southern and southwestern Europe, partly due to a projected decrease in cyclone frequency in the Mediterranean [45].

In spite of potentially large societal impacts, mechanisms involved in changes in frequency and intensity of heavy precipitation are much less explored. The purpose of this article is to improve techniques for predicting these extreme precipitation events and to advance our knowledge of the possible mechanisms whose incidence and intensity are linked to global warming. For this, we will analyze in detail the different phases of hydroclimatic mechanisms that led to an extreme precipitation event in Germany in July 2021, that is, a region reputed not to be floodable, causing many casualties.

1.3. Oceanic Rossby Waves at Mid-Latitudes

Oceanic Rossby waves have a well-known effect on the climate. The role of Rossby waves in local air-sea interactions over the tropical Indian Ocean and in remote forcing from the tropical Pacific Ocean has been investigated during El Niño and positive Indian Ocean Dipole years [46,47]. High-resolution subsurface observations have provided insight into equatorial oceanic Rossby wave activity forced by Madden-Julian Oscillation events [48].

However, the role played by the oceanic Rossby waves on the climate is not limited to the tropical oceans. The Rossby waves that develop where the western boundary currents leave the continents to re-enter the subtropical gyres have a strong impact on climate [31]. Located at the same latitudes as the subtropical jet streams, they thus participate in the cyclogenesis of mid-latitude eddy systems (anticyclones and depressions) then moving under these powerful air currents.

Oceanic Rossby waves propagate westward. Being approximately non-dispersive, their phase velocity given by the dispersion relation only depends on the latitude [49]. The phase velocity decreases when the latitude increases. At mid-latitudes, it is lower than the velocity of the eastward propagating wind-driven current of the gyre resulting from Ekman pumping associated with the wind curl. Rossby waves are driven by the circulation of the gyre.

Based on the momentum equations of Rossby waves, these baroclinic waves are forced by changes in solar irradiance induced by solar and orbital cycles [50,51]. This property is specific to Rossby waves at mid-latitudes because, in tropical oceans, they are mainly driven by the wind, in this case the trade winds. Under the effect of radiative forcing, in addition to a Sea Surface Height (SSH) anomaly, the propagation of Rossby waves along the subtropical gyre induces a zonal and a meridional modulated current. The meridional current is in phase with the forcing while the zonal current and the SSH perturbation, i.e., the ridge of the Rossby wave, are in quadrature. During the ascending phase of the zonal ridge, the meridional modulated currents converge toward the ridge.

The convergence causes the thermocline to deepen due to the inflow of warm water from the surface of the ocean. The affected ocean surface extends well beyond the gyre due to the meridional currents. A quarter of a period later, the zonal modulated current reaches its maximum at the same time as the ridge. The zonal currents are in opposite phase on either side of the ridge, causing the zonal propagation of the thermocline wave.

Both the meridional and the zonal modulated current change direction every half-period. Note that the speed of the zonal current is expressed in a relative way because the westward propagating Rossby wave is carried by the eastward propagating wind-driven current of the gyre. Its absolute speed is obtained by adding it to that of the steady wind-driven current. Thus, the zonal current of the gyre periodically accelerates, slows down, and sometimes even reverses direction.

During its ascending phase, the Rossby wave behaves like a heat sink while, during its recession phase, the upwelling which occurs along the ridge causes the Rossby wave to release heat that has been stored when the thermocline was lowering. This explains the climatic impact of Rossby waves at mid-latitudes; sometimes they favor high-pressure systems, sometimes low-pressure.

2. Materials and Methods

2.1. The Caldirola–Kanai Oscillator

Several Rossby waves of different periods overlap along the gyre. Sharing the same zonal and meridional modulated currents, these Rossby waves behave like coupled oscillators with inertia. The equation of the Caldirola–Kanai (CK) oscillator, which is a fundamental model of dissipative systems that is usually used to develop a phenomenological single-particle approach for the damped harmonic oscillator [52], can be expressed by considering the conditions of durability of the dynamic system. For that, the equation of the CK oscillator is formulated to express the mode of coupling between N Rossby waves that share the same modulated geostrophic currents [50]:

$$\mathcal{M}_i\ddot{u}_i + \gamma\mathcal{M}_i\dot{u}_i + \sum_{j=1}^{N} J_{ij}\left(u_i - u_j\right) = I_i\cos(\Omega t) \tag{1}$$

where u_i is the zonal geostrophic current velocity of the ith oscillator along the gyre, $\mathcal{M}_i$ the mass of water displaced during a cycle resulting from the quasi-geostrophic motion of the ith oscillator, γ the Rayleigh friction, and J_{ij} the measure of the coupling strength between the oscillators i and j. The right-hand side represents the periodic driving on the ith oscillator with frequency Ω and amplitude I_i, that is, Coriolis and pressure gradient forces. The restoring force simply depends on the difference in velocity of zonal geostrophic currents between the oscillators. So, it vanishes when the velocities are equal $u_i = u_j$ which, in the absence of friction, removes any interaction between the oscillators i and j. On the other hand, the strength of the interaction increases as the difference in velocities increases. The coupling of Rossby waves is exercised by the fact that the velocities u_i are common at the convergence of the modulated geostrophic currents of the resonant oscillatory system.

In order to ensure the durability of that dynamic system, the coupled oscillators have to form oscillatory subsystems so that the resonance conditions are defined recursively:

$$\tau_i = \frac{1}{n_i}\tau_{i-1} \text{ with } \tau_0 = T \tag{2}$$

where $n_i = 2$ or 3. T is the period of the fundamental wave, that is, one year.

The CK oscillators resonate in subharmonic and harmonic modes of the annual fundamental wave. The apparent eastward propagation velocity of this fundamental wave depends on the latitude of the gyre where the western boundary current leaves the continent, and to the velocity of the steady wind-driven current. In the case of a pseudo-periodic forcing, its apparent wavelength is adjusted to the forcing period when the average forcing frequency is present in the frequency spectrum of the dynamic system. Natural frequencies close to the forcing frequency are favored, while those far from it are dampened because

of friction so that the fundamental wave is resonantly forced by the variations in solar irradiance resulting from the declination of the sun. This is by far the primary source of temperature variability in surface and subsurface waters of the oceans at mid-latitudes.

2.2. Data

Daily gridded data (1/4 degree × 1/4 degree) of SSH, geostrophic currents [53], and SST [54–57] are used. SSH and geostrophic current data begin 15 March 2019. Although starting earlier, SST data is used over the same time interval as SSH. The last update was on 17 October 2021.

Data of precipitation is produced as part of the Global Precipitation Climatology Project (GPCP) Climate Data Record (CDR) Daily analysis, which spans the time period October 1996 to the near present [58,59]. The algorithm to produce the daily 1° GPCP product takes inputs from several different sources and merges them to create the most consistent and accurate daily precipitation estimates [60].

2.3. Wavelet Analysis

2.3.1. Marine Heatwaves

The problem that we are going to tackle, which relates to the genesis of MHWs at mid-latitudes, consists in highlighting the evolution of brief SST anomalies at different time scales, reflecting the driving role of oceanic Rossby waves. A Morlet cross-wavelet analysis is performed to estimate the amplitude of variations in characteristic period bands of four state variables, that is, SSH, modulated geostrophic currents, and SST, as well as their phase compared to a reference time series [61]. Presently, SST averaged along the parallel 34.125° N, between 145.625° E and 148.125° E, is used as the time reference. The average of the SST data over a short segment of the parallel makes it possible to specify the evolution of the heat wave over time by reducing the noise without significantly harming the spatial resolution from which the location of the reference is defined.

As we will see later, SST anomalies observed on 5 January 2020 and on 23 July 2021 are representative of a phenomenon that led to a "marine cold wave" in the first case and a "marine heatwave" in the second. This time reference is chosen so that it unambiguously reflects those two extreme events, both being defined as a sharp surface temperature anomaly (the extremum does not last more than a day), positive or negative as the case may be.

Under these conditions, the square root of the wavelet power applied to the state variable time series, scale-averaged over the period bands, is the regionalized amplitude of anomalies, whatever their date of occurrence. The cross-wavelet power applied to both the state variable time series and the time reference, scale-averaged over the period bands, is the regionalized phase of anomalies. It is the time-lag between the extrema of the anomalies and the date of occurrence of the extreme event, namely the marine cold wave or the MHW [62]. Consequently, for each state variable and for each period band a paired map of the amplitude and the phase of anomalies is obtained.

The wavelet analysis of the state variables is carried out over short periods of time framing the date of occurrence of the extreme events. In this way, for each band, both the amplitude and the phase of the anomalies are time-averaged over a time interval coinciding with the width of the band, centered on the date of occurrence of the extreme events.

The choice of each period band is guided by the properties of the CK oscillator considered as a prototype of coupled Rossby waves. Harmonics of the CK oscillator are identifiable in Figure 1b that represents the Wavelet Fourier spectrum of SSH at 34.125° N, 140.125° E located on the north Pacific gyre, 0.75° south of the Pacific shelf off the southeastern region of Japan. The richness of the Fourier spectrum is probably attributable to the proximity of the coasts of Japan facing the Pacific Ocean. This suggests a local resonance of Rossby waves, which strengthens harmonics. The Fourier spectrum distinctly shows the annual fundamental wave, the amplitude of which is predominant, which gives rise to harmonics whose main periods are 1/3 yr, 1/6 yr, 1/12 yr, and 1/24 yr.

Rossby waves are subject to very large fluctuations as attested by the width of the peaks in the Fourier spectrum. Only the amplitudes of the harmonics whose periods are 1/12 yr and 1/24 yr are known with a level of confidence greater than 95% (the lack of precision of the amplitude of the annual Rossby wave results from the short duration of the observation period, which was barely 3 years).

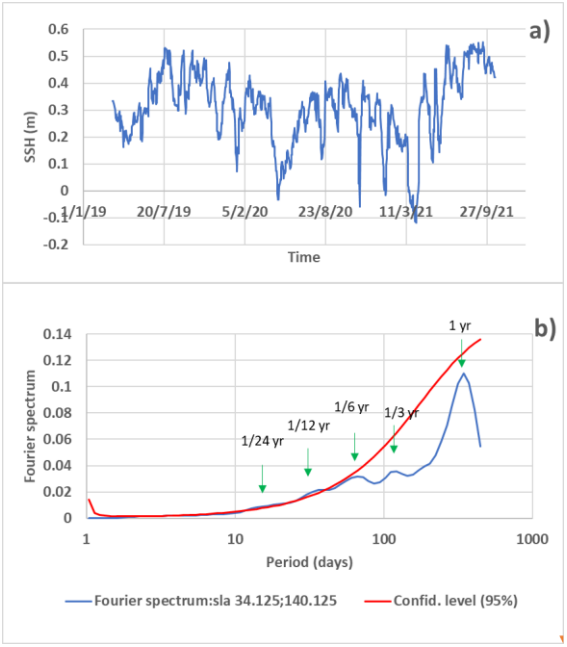

Figure 1. The SSH anomaly at 34.125° N, 140.125° E–(**a**) the raw signal–(**b**) the Wavelet Fourier spectrum (adimentional) and the main harmonics. SSH data is provided by the National Oceanic and Atmospheric Administration (NOAA) https://coastwatch.noaa.gov/pub/socd/lsa/rads/sla/daily/nrt/ (accessed on 27 April 2022).

In Table 1 the period bands are chosen in accordance with (2). Bandwidths are deduced from the mean period τ of harmonics. Lower and upper limits are $0.75 \times \tau$ and $1.5 \times \tau$, respectively, so that the bands are contiguous, since the periods are halved from one harmonic to another. The progression of the bands is continued beyond the periods analyzed (mean periods 1/48 and 1/96 years).

Table 1. Properties of observed or presumed harmonics and bandwidths.

Harmonic	n_i from (1)	Mean Period (Days)	Lower Limit (Days)	Upper Limit (Days)
1	_	365.2	_	_
1/3	3	121.7	91.3	182.6
1/6	2	60.9	45.7	91.3
1/12	2	30.4	22.8	45.7
1/24	2	15.2	11.4	22.8
1/48	2	7.6	5.7	11.4
1/96	2	3.8	2.9	5.7

2.3.2. Subtropical Cyclones

The phenomenological study of climatic phenomena leading to extreme precipitation at mid-latitudes is performed in the same way. Three state variables are jointly analyzed, the precipitation height, i.e., the thickness of the layer of water produced during a day, SST, and SSH. When a positive SST anomaly is locally in phase with the extreme precipitation event while being within the perimeter of the cyclonic low-pressure system, this means that the water vapor evaporated from the ocean is involved in the cycle of cyclogenesis by providing latent heat during the condensation process. This concomitance results from the

fact that the atmospheric phenomena leading to the transport of water vapor within the low-pressure system are very rapid compared to the oceanic processes at the origin of the SST anomalies. As will be justified later, the supply of the cyclonic system from the free surface of the ocean occurs in less than a day, whereas the maturation of a large surface and uniform phase SST anomaly generally takes at least ten days.

3. Results

3.1. Marine Heatwaves

As shown in Figure 2c,d sudden positive or negative SST anomalies may occur where Rossby waves are resonantly forced [1]. Two major positive anomalies occurred during the time of observation, namely from 1 January 2019 to 27 September 2021. The first positive anomaly occurred on 30 May 2019, the second on 23 July 2021. The first is one month ahead of the corresponding negative SSH anomaly, while the second is 2 weeks in advance (Figure 2a,c). Anticipation of SST anomalies means that they occurred while the thermocline was lifting. One major negative SST anomaly occurred on 5 January 2020, one week behind the corresponding positive SSH anomaly, while the thermocline was deepening (Figure 2b,d).

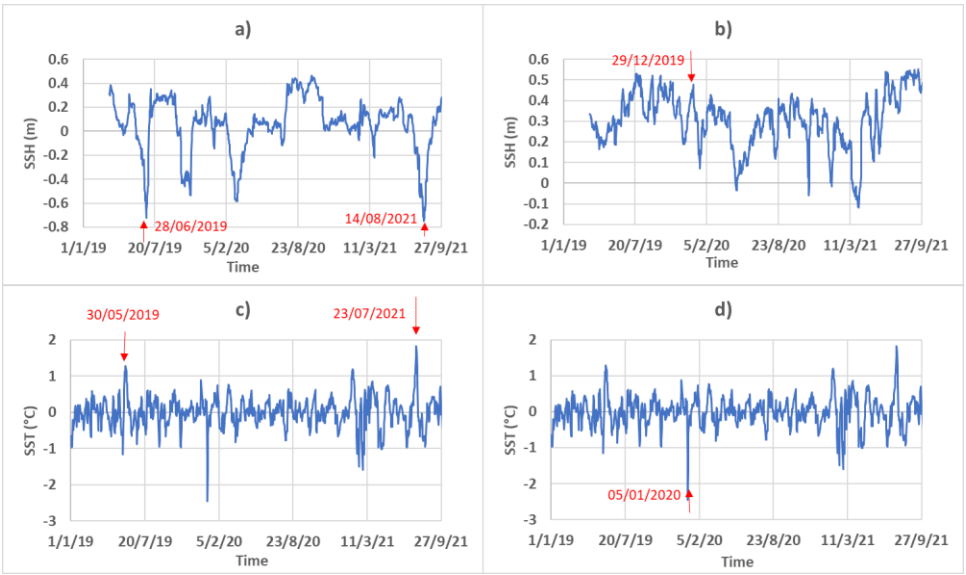

Figure 2. Abrupt events highlighted by SSH at 34.125° N, 148.125° E in (**a**) and at 34.125° N, 140.125° E in (**b**), and by SST averaged along the parallel 34.125° N between 145.625° E and 148.125° E, and filtered in the band of 1–68 days to emphasize the rapid variations while attenuating the annual variations. This series is used as the time reference in the wavelet analysis of data. (**a**,**c**) are referring to warm events, (**b**,**d**) to cold events. SST data is provided by NOAA https://www.ncei.noaa.gov/data/sea-surface-temperature-optimum-interpolation/v2.1/access/avhrr/ (accessed on 27 April 2022).

Each SST anomaly corresponds to an opposite SSH anomaly. The reverse is not true; some SSH anomalies do not produce significant SST anomalies. This suggests strong ocean–atmosphere interactions are required for the Rossby waves to produce coherent SST anomalies, with a threshold effect.

3.1.1. The Marine Heatwave That Occurred on 21 July 2021

The climatic impact of this heatwave was significant. One of the most notable records in July 2021 was registered in Asahikawa 43°46′ N, 142°22′ E [63]. The city registered 36.2 °C on 27 July, breaking the previous record of 36 °C set on 7 August 1989.

3.1.2. Wavelet Analysis of Climatic State Variables

As shown in Figure 3a,c,e,g,i, the harmonics of SSH are visible along the North-Pacific gyre, mainly between latitudes 25° N and 35° N, and between longitudes 130° E and 180°. The longitudinal and meridional extensions of Rossby waves increases with period. With regarding to the harmonic 1/6, the SSH anomaly in Figure 3i,j extends over areas of the northwestern Pacific Ocean, including the Yellow Sea, and the entire Sea of Japan.

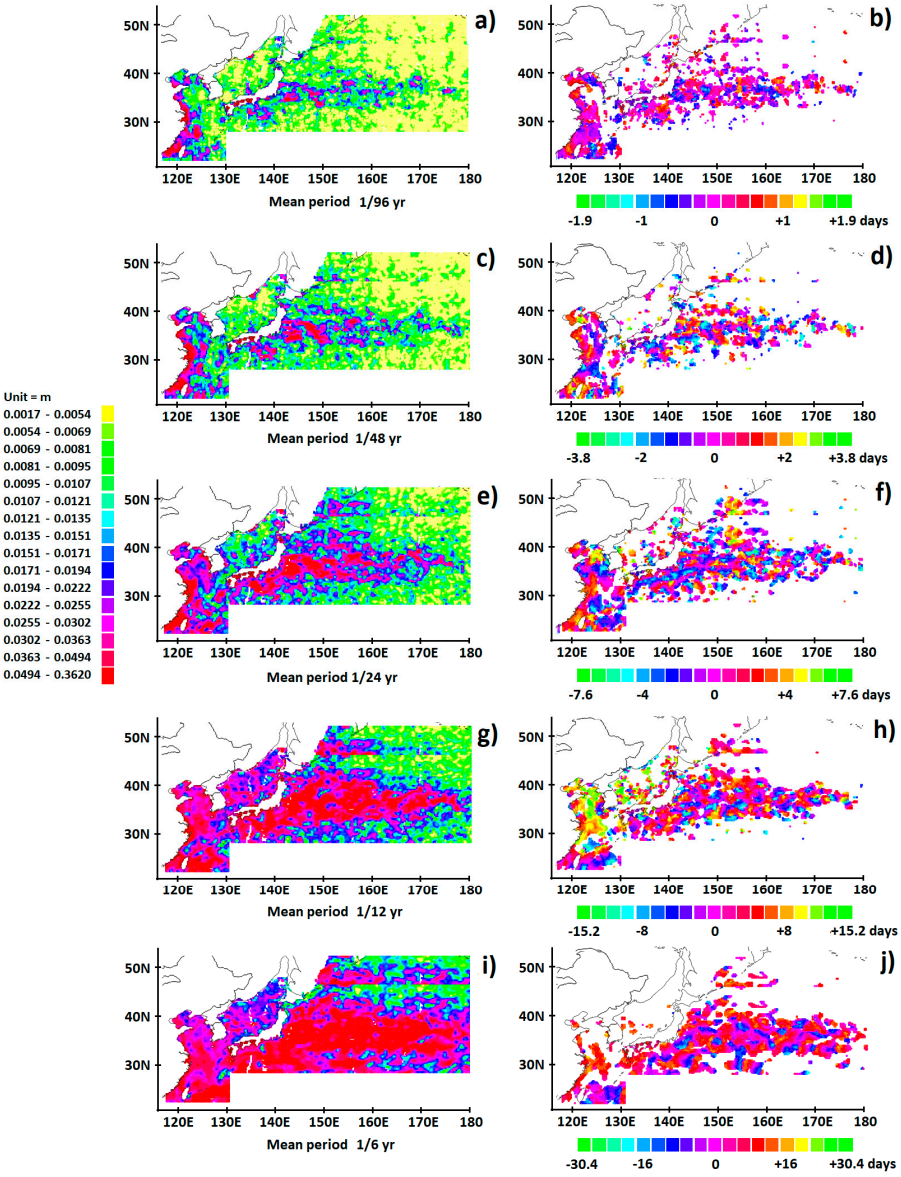

Figure 3. The amplitude (**a**,**c**,**e**,**g**,**i**) and the phase (**b**,**d**,**f**,**h**,**j**) of the harmonics of SSH. The periods are 1/6 yr in (**a**), (**b**) 1/12 yr in (**c**), (**d**) 1/24 yr in (**e**), (**f**) 1/48 yr in (**g**), and (**h**) 1/96 yr in (**i**,**j**). The amplitudes are expressed in 16 classes, each containing the same number of individuals (quantiles). The color of the bar associated with the phase represents an angle varying from −180° to + 180° [61] (each class corresponds to 20°). This angle is reflected by a segment of time of one period, hence the coincidence of the colors at the ends. Time lags in (**b**,**d**,**f**,**h**,**j**) are relative to 23 July 2021. The time reference is the SST anomaly averaged along the parallel 34.125° N between 145.625° E and 148.125° E. The SSH anomaly is negative when the time lag is zero (the SSH anomaly is negatively correlated with the SST anomaly and late compared to SST). Only the phase corresponding to the 37.5% quantile of the highest values of the amplitude is displayed. Same data sources as in previous figures.

In Figure 3b,d,f,h,j, the phase of the SSH anomaly clearly shows a succession of ridges and troughs in phase opposition. The momentum equations applied to a quasi-geostrophic motion of oceanic Rossby waves show that the meridional geostrophic current V is in phase with the forcing while both the zonal current U and SSH anomalies are in quadrature. However, the phase is more precise for the zonal current (Figure 4) and the meridional current (Figure 5) than for SSH in Figure 3. Indeed, the estimation of geostrophic current velocities from SSH anomalies has a filtering effect because it involves surrounding measurements of SSH. This has the effect of reducing noise and making the interpolated values more representative than the raw measurements of SSH.

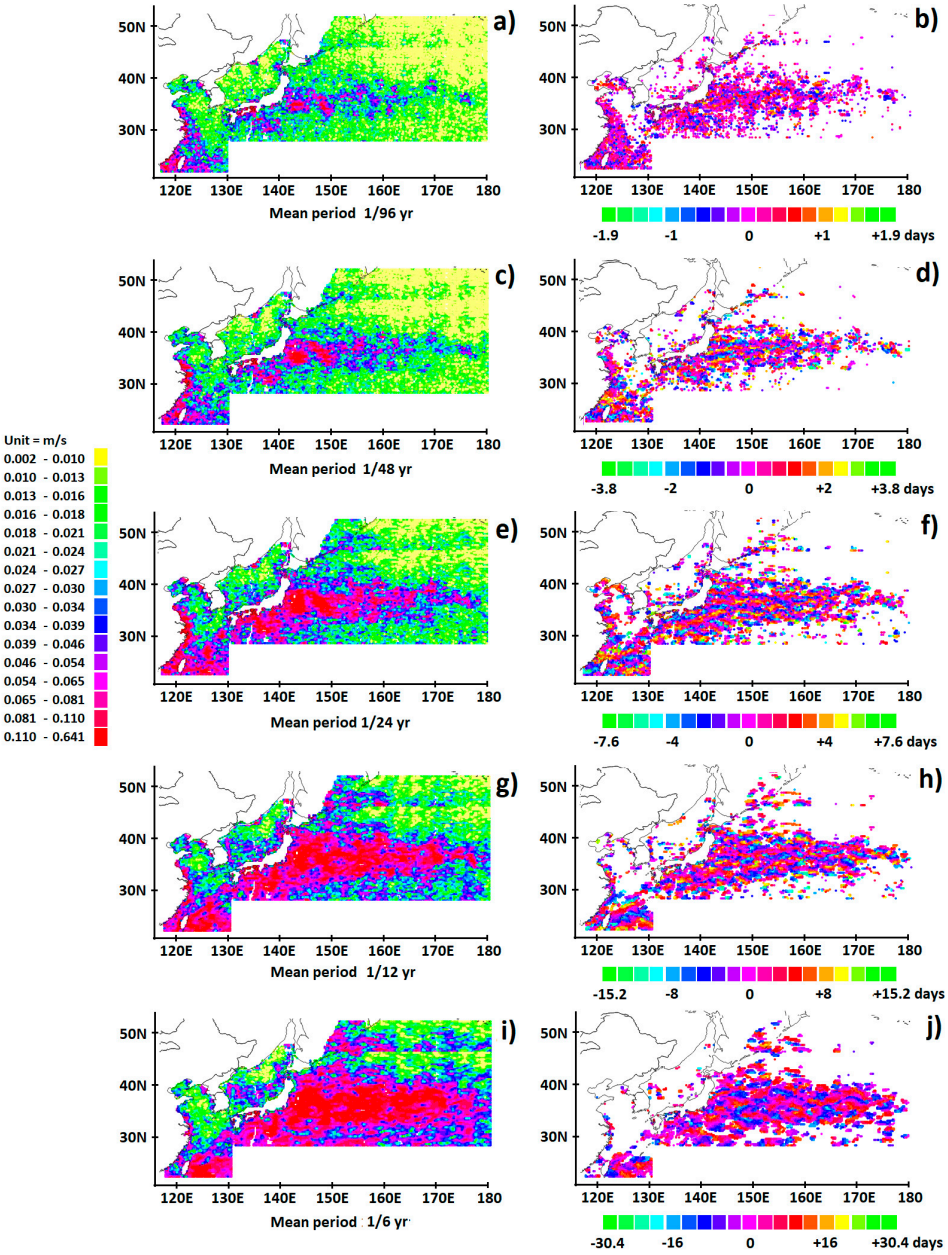

Figure 4. Same as Figure 3 for the amplitude (**a**,**c**,**e**,**g**,**i**) and the phase (**b**,**d**,**f**,**h**,**j**) of the zonal geostrophic current U oriented to the east when the time lag is zero. Same data sources as in previous figures.

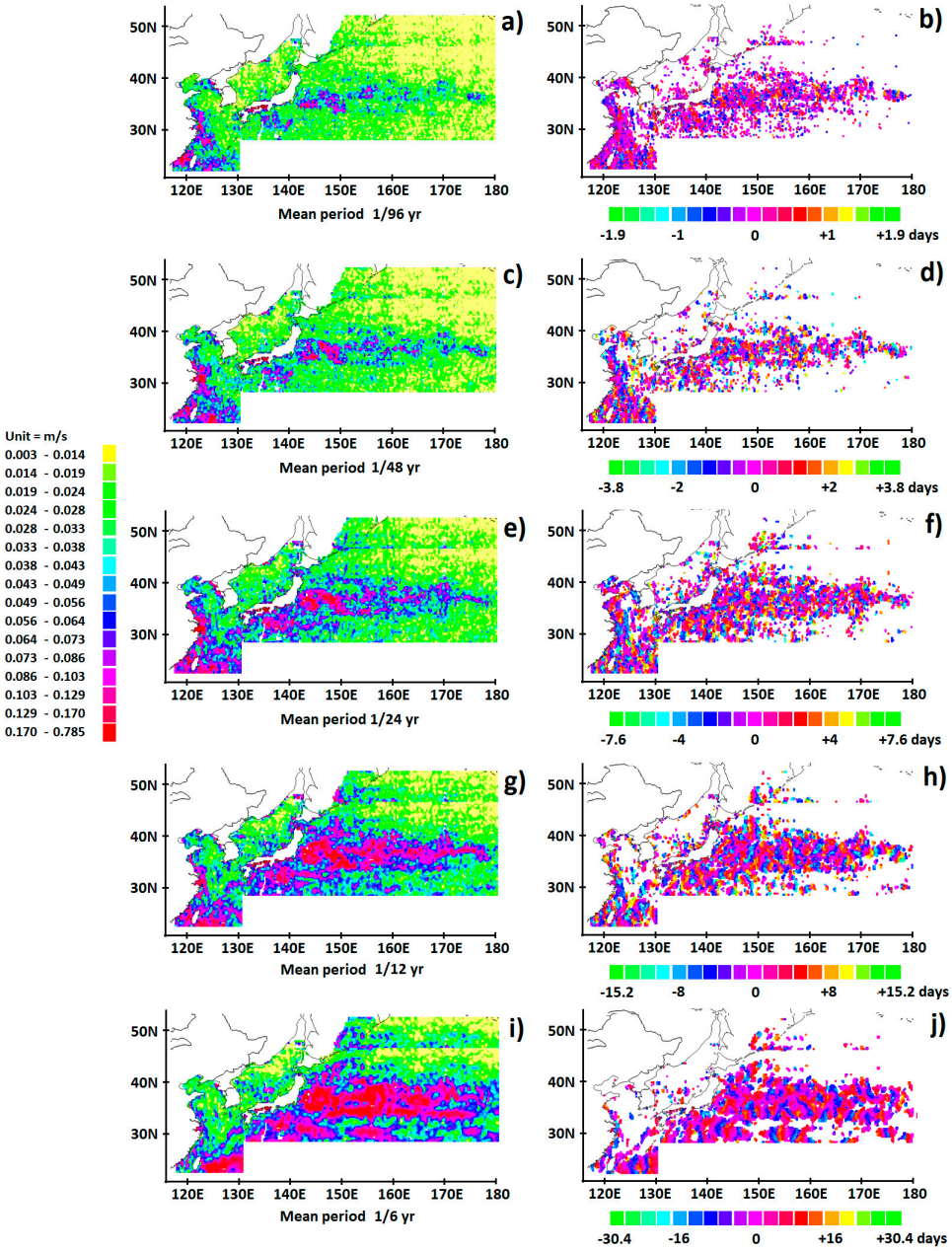

Figure 5. Same as Figure 3 for the amplitude (**a**,**c**,**e**,**g**,**i**) and the phase (**b**,**d**,**f**,**h**,**j**) of the meridional geostrophic current V oriented to the south when the time lag is zero. Same data sources as in previous figures.

The modulated geostrophic currents change direction every apparent half-wavelength of Rossby waves. Thus, in Figure 4, the zonal current U shows a succession of regions in phase opposition whose size corresponds to an apparent half wavelength of Rossby waves. These regions form a mosaic of cells in which the zonal geostrophic currents converge or diverge when the cell is translated longitudinally by half of a wavelength. This alternation is still observable for meridional current V (Figure 5), but this time convergence or divergence occur in the North-South direction.

Figures 4 and 5 confirm the previous observations regarding the longitudinal and meridional extensions of Rossby waves along the gyre from SSH as the period increases. This also applies to the speed of modulated geostrophic currents. However, the anomalies of modulated geostrophic currents remain localized along the gyre as the period increases, without stretching to the Yellow Sea, and the Sea of Japan, as does SSH. This difference in

the behavior of Rossby waves in the semi-closed seas suggests that these seas are not large enough to allow the formation of perceptible geostrophic currents.

Anomalies in opposite phase also widen with the period, consistent with the increase in apparent Rossby wavelength. The anomalies of the zonal component of the geostrophic current U extend longitudinally with the period while the anomalies of the meridional component V extend latitudinally as shown in Figures 4j and 5j.

Downwelling that occurs in convergent cells means that the thermocline lowers, the intake of warm water resulting from geostrophic currents. On the contrary, upwelling that occurs in divergent cells makes the thermocline rise, restoring warm water under the effect of geostrophic currents. The alternation of convergent or divergent cells throughout the gyre at mid-latitudes highlights the determining role of these cells regarding their climatic impacts. These privileged ocean–atmosphere interactions along the gyre occur at all time scales extending from the annual, seasonal cycles to time intervals not exceeding a few days.

These ocean–atmosphere interactions induce atmospheric baroclinic instabilities as suggested by the variations in SST at the rate of the different periods of the Rossby waves, as shown in Figure 6. The transient SST anomalies occur along the gyre from which the Kuroshio leaves the Asian continent to a longitude close to 180°. Regarding the harmonic 1/6, the SST anomaly in Figure 6i,j is translated over extensive areas of the northwestern Pacific Ocean, including the Yellow Sea, the entire Sea of Japan, and part of the Sea of Okhotsk, as does SSH.

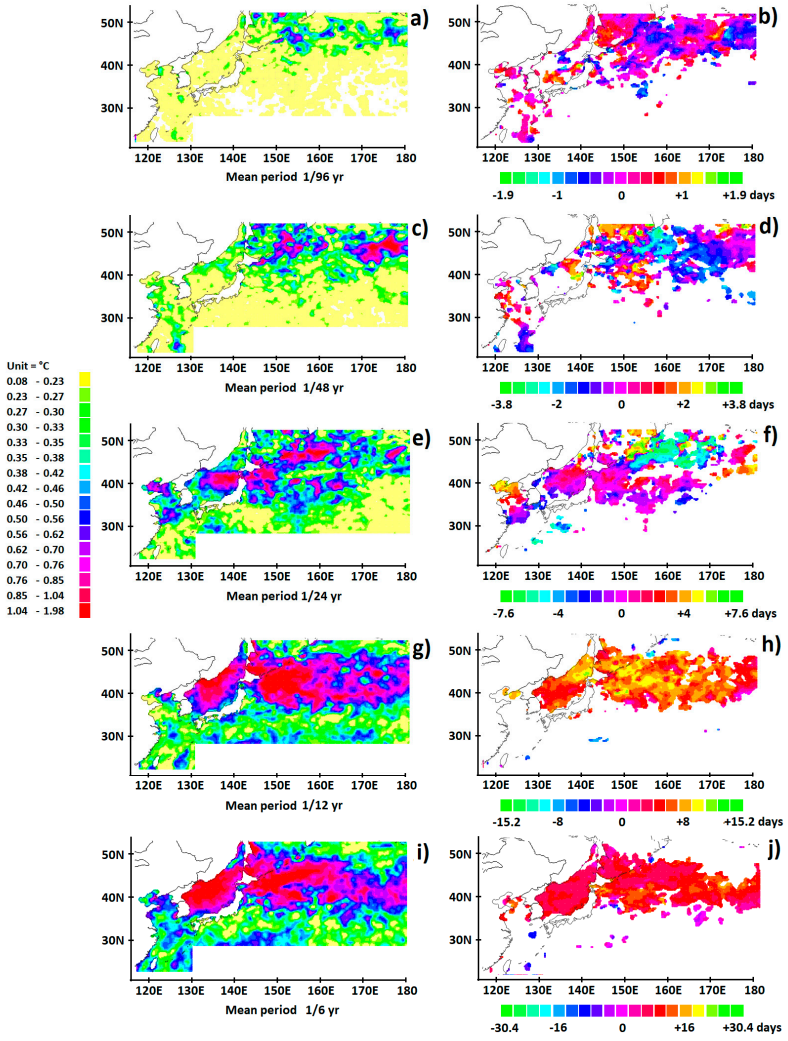

Figure 6. Same as Figure 3 for the amplitude (**a**,**c**,**e**,**g**,**i**) and the phase (**b**,**d**,**f**,**h**,**j**) of SST whose anomalies are positive when the time lag is zero. Same data sources as in previous figures.

Compared to SSH, SST anomalies are translated to the north while widening (Figure 6). This translation that appears especially during the first 3 periods is of short duration, which suggests the role of the atmosphere. Highly contrasted during the first 3 periods, the phases of SST anomalies become uniform as the period increases. As shown in the Figure 6j, uniformity of the phase is achieved for the harmonic 1/6, which confirms that the lifetime of the SST anomaly is very short compared to the period close to 2 months.

3.2. The Marine Cold Wave That Accurred on 5 January 2020

Figure 7 shows the amplitude and the phase of SST anomalies during the cold event. Anomalies are little translated toward the north, which suggests the weakness of the SST response to the meridional component of the wind resulting from a high-pressure system initiated by the negative SST anomaly of the gyre. Here again, the phase shows a mosaic of convergent and divergent cells characterized by the inversion of geostrophic currents (Figure 7d,f). But contrary to what happens for MHWs, the phase does not homogenize when the period increases, reflecting the SSH anomaly. This suggests the weakness of the ocean–atmosphere interactions, hence the weak climatic impact of marine cold waves.

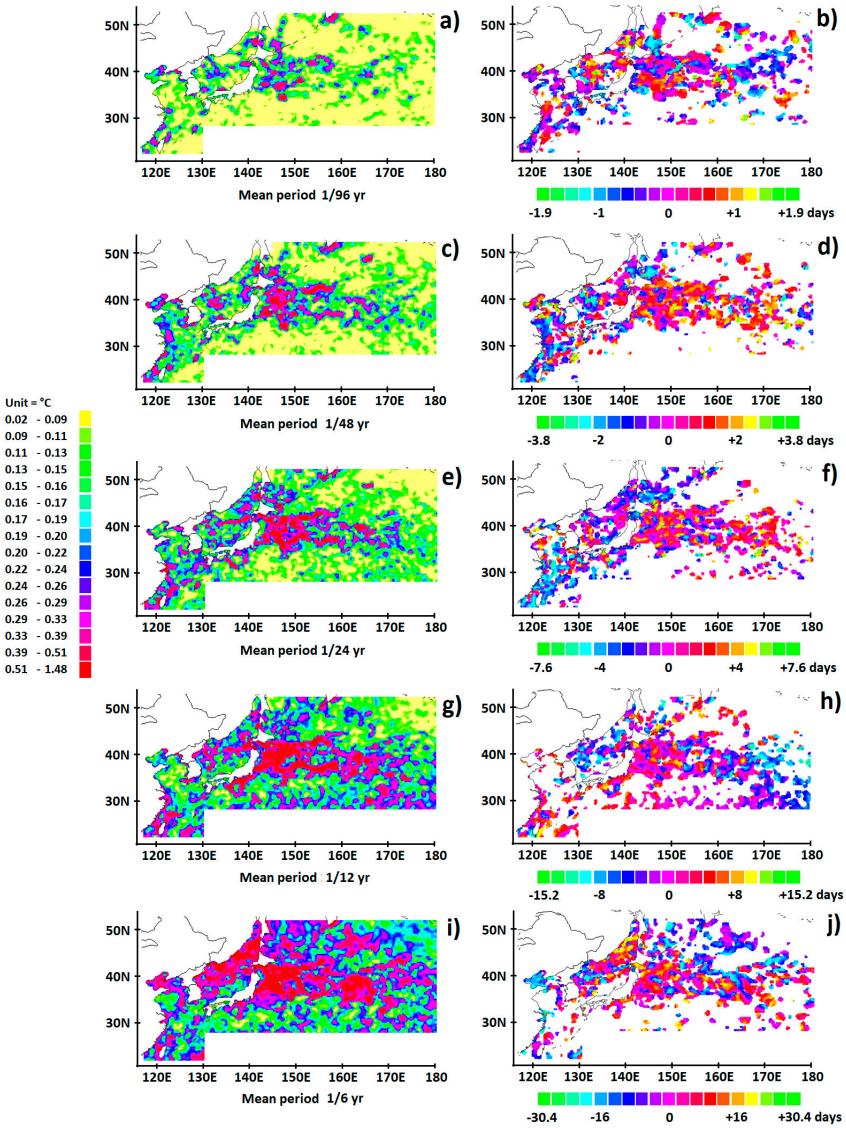

Figure 7. Same as Figure 3 for the amplitude (**a**,**c**,**e**,**g**,**i**) and the phase (**b**,**d**,**f**,**h**,**j**) of SST whose anomalies are negative when the time lag is zero. Time lags in (**b**,**d**,**f**,**h**,**j**) are expressed in relation to 5 January 2020. Same data sources as in previous figures.

3.3. Subtropical Cyclones

Subtropical cyclones develop at mid-latitudes around a stationary front due to an upper-level disturbance, generally an upper-level trough downstream of a strong westerly jet [63,64]. Cyclogenesis results from the combination of vorticity advection and thermal advection created by the latitudinal temperature gradient, a low-pressure center causing upward motion around the low [65]. This rotational flow will push polar air equatorward west of the low via its cold front, and warmer air will push poleward low via the warm front.

3.3.1. An Extreme Precipitation Event, Germany, July 2021

During one week in July 2021, severe flooding occurred across Europe due to dangerous thunderstorms and rain, hitting Germany the hardest. This country experienced up to 182 mm of rain within 72 h. More than 170 people have lost their lives and entire communities have been destroyed. The number of victims of this flood disaster exceeds that of all previous inland floods in Germany since 1900 combined [66].

In mid-July 2021, a pronounced high altitude low shifted from France to the Alps and southern Germany. On its front, very warm and humid air masses were directed to the north and east of Germany, concomitantly with fresher Atlantic air to the south and south-west of Germany, causing record rainfall in parts of North Rhine-Westphalia and Rhineland-Palatinate.

3.3.2. Wavelet Analysis of State Variables

Precipitation height is represented in Figure 8. Here again, the low-pressure system is decomposed into the 5 period bands, the time shift of precipitation areas being relative to the date of occurrence of the extreme rainfall event on 14 July 2021.

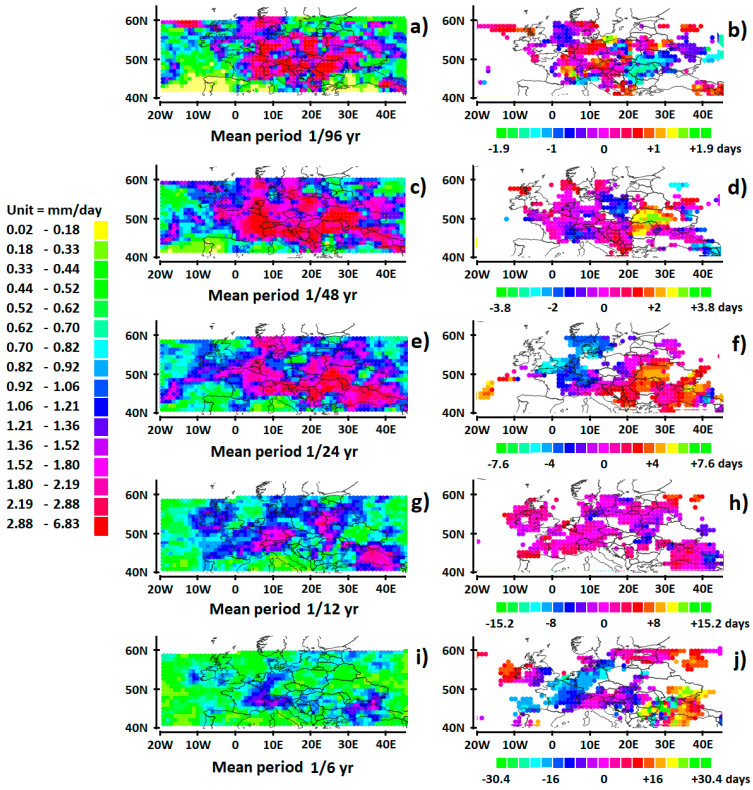

Figure 8. Same as Figure 3 for the amplitude (**a**,**c**,**e**,**g**,**i**) and the phase (**b**,**d**,**f**,**h**,**j**) of the harmonics of the precipitation height in western Europe. Time lags in (**b**,**d**,**f**,**h**,**j**) are expressed in relation to 14 July 2021. The time reference is the rainfall height in Germany at 47° N, 18° E. Daily precipitation data is provided by NOAA https://www.ncei.noaa.gov/data/global-precipitation-climatology-project-gpcp-daily/access/ (accessed 27 April 2022).

The two main precipitation areas represented in Figure 8i,j, i.e., within the band centered on the period 1/6 yr, are independent since they are strongly out of phase with each other. In contrast, Figure 8g,h highlights a coherent low-pressure system at the synoptic scale within the band centered on the period 1/12 yr. The phase of the three main rainfall areas over central and western Europe are indeed only slightly shifted.

According to Figure 8e,f, the rotation of the low-pressure system occurs within the period band centered on 1/24 yr. This deduction is based on the presence of two rainfall areas in phase opposition on both sides of the disaster area, which confirms the hypothesis that the different rainfall areas belong to the same dynamic system at a synoptic scale. The cyclonic flow is fed mainly by the Atlantic west of the coasts of western Europe (Figure 9g,h) and the Baltic Sea (Figure 9e,f).

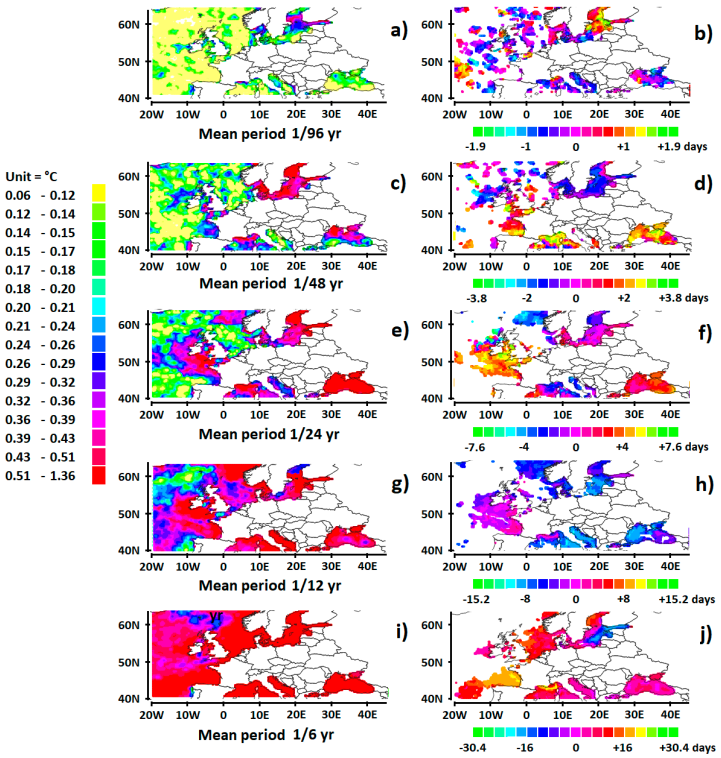

Figure 9. Same as Figure 8 for the amplitude (**a**,**c**,**e**,**g**,**i**) and the phase (**b**,**d**,**f**,**h**,**j**) of SST. SST anomalies are positive when the time lag is zero. Same data sources as in previous figures.

An SST anomaly over the Atlantic west of the coasts of southern England, Ireland, and France does indeed occur within the period band centered on 1/12 yr (Figure 9g,h), reaching more than 1 °C. The phase of this anomaly is close to zero, showing that ocean–atmosphere interactions are occurring while the SST anomaly is peaking. With regard to the Baltic Sea, the SST anomalies peak within the period bands centered on 1/48 and 1/24 yr, as shown in Figure 9c–f. The phase of the anomaly is close to zero within the period band centered on 1/24 yr, while it is slightly shifted negatively within the period band centered on 1/48 yr, but it nevertheless contributes significantly to the feeding of the low-pressure system by peaking the day before the extreme event occurred.

In the Baltic Sea, SST increases when SSH decreases, i.e., when the thermocline rises. This phenomenon is mainly observable within the period band centered on 1/24 yr (Figures 9e,f and 10e,f) where the phase of the SST anomaly is close to zero. The phases of both SSH and SST anomalies are uniform in seas bordered by coasts, which modifies the apparent wavelength of Rossby waves. It is elongated, in this case, in the absence of a strong current flowing east in which Rossby waves would be embedded. The latter result from the declination of the sun and the variation in solar irradiance during the year, which induces the motion of the thermocline. The westward propagating Rossby waves and their

harmonics remain confined in these seas. Convection processes occur in subsurface water, favoring the warming of surface water. These conditions are conducive to the formation of baroclinic instabilities in the atmosphere as a result of increased evaporation.

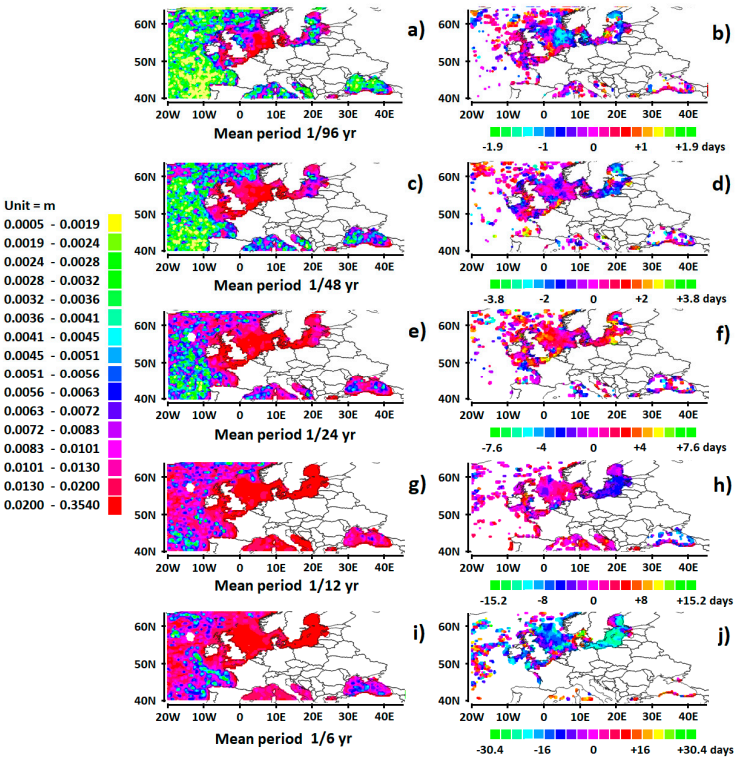

Figure 10. Same as Figure 8 for the amplitude (**a**,**c**,**e**,**g**,**i**) and the phase (**b**,**d**,**f**,**h**,**j**) of SSH. SSH anomalies are negative when the time lag is zero. Same data sources as in previous figures.

With regard to the Atlantic Ocean, SSH anomalies are weak off the coasts of western Europe, whereas the amplitude of SST anomalies is high. This suggests that this temperature anomaly results from atmospheric phenomena that translate the SST anomalies developing along the North Atlantic gyre toward the east, a process that leads to baroclinic instabilities in the atmosphere.

As shown in Figure 8a–f, the size of the cyclonic flow reduces as the mean period decreases from 1/24 to 1/96 yr, remaining centered in Germany while the rotation accelerates. Within the period band centered on 1/96 yr, the precipitation area is concentrated between latitudes 45° N and 55° N, and longitudes 3° E and 20° E. East of 20° E the precipitation does not contribute to the genesis of the extreme event since it is strongly out of phase (Figure 8b). In addition, the phase is uniform, close to zero, within sampling errors (the step is daily).

Figure 8b,d,f show that several atmospheric layers are rotating simultaneously. They concentrate around the disaster zone as the rotation accelerates. The half-period of rotation passes from the order of 4 days (Figure 8f) to a few hours (Figure 8b). Since the precipitation areas concentrate around the axis of rotation of the low-pressure system while the rotation period decreases, this suggests that the rotation is accelerating as the layer rises, driven by the upward flow of the cyclonic system. In this way, the uppermost layer is fed by the lower layers. Its phase is uniform so that the rotation period is less than the duration of the extreme precipitation event. The water vapor contained in the different atmospheric layers condenses when they rise due to the lowering of the temperature, which leads to heavy precipitation.

However, the concentration of precipitation, which occurs during cycles of shorter periods, cannot be approached using the same data, which is beyond the scope of this article. Here, the spatial and temporal resolution of the rainfall data [60] are suited to highlighting

the various stages leading to the deepening of the low-pressure system, namely the merging of the various low-pressure systems at the synoptic scale, and the feeding of the cyclonic flow from the Atlantic Ocean off the coasts of western Europe and the Baltic Sea.

4. Discussion

4.1. Marine Heatwaves

Regarding MHWs, uniformization of the phase as the SST anomaly migrates north only becomes mature in the 1/6 harmonic mode. In the 1/12 mode, the maturation of the SST anomaly is not complete, a time shift of the order of one week remaining within the anomaly (Figure 6h).

With regard to short cycles corresponding to harmonic modes 1/24, 1/48, and 1/96, the northernmost fringe of the SST anomaly whose phase is heterogeneous is transient. Indeed, it disappears completely during long cycles, the SST anomaly concentrating around a zonal midline at approximately 42° N (Figure 6j). This suggests that the warm, humid air from the low-pressure system warms the sea surface as it migrates north, inducing convective processes in subsurface water while the SST becomes increasingly cold. This promotes the creation of a vertical profile of convection/evaporation tending toward an equilibrium between the thermocline and the surface of the ocean. But stratification of the subsurface water leading to this vertical profile seems unstable and does not occur systematically, as shown in Figure 2.

This strong ocean–atmosphere interaction which causes the thermocline to rise, could explain the uniformization of the phases of the SST anomalies at latitudes where the northward thermal gradient of surface water is steep. Uniformization of the phases then amounts to assuming an overall movement of the thermocline during the longest cycle, hence the brief but intense heatwave which appeared around 27 July 2021.

The northward translation of the SST anomaly is only significant in the case of heatwaves due to the low-pressure system that forms above the gyre before developing into a synoptic cyclonic system. This enhances the SST response to latent and sensible heat fluxes directed to the north. This sudden SST response to atmospheric transfers has already been observed, which sparked interest in this research [21]. According to the authors, MHW observed at the sea surface in the summer of 2021 was the largest in extent and intensity since the beginning of satellite measurements of global SST in 1982, with a strong societal impact.

Other works reported such MHWs in the northwestern Pacific [9,22]. Ref. [22] reported the positive SST anomaly that occurred in August 2020 in subtropical waters in the surroundings of the gyre 120° E–180° E, 20° N–35° N, which was attributed to anthropogenic forcing. Further investigations seem necessary to validate such a hypothesis. Indeed, this positive SST anomaly does not seem distinguishable from internal variability in the context of the present study (Figure 2c).

In [17] the SST of the Oyashio region abruptly increased in the summer of 2010, and a high summertime SST repeated every year until 2016. This was attributed to the strengthening of the Kuroshio water influence. In [9], extreme weather and MHWs are reported; these occurred simultaneously around the Pacific shelf off southeastern Hokkaido, Japan. In these two cases, the influence of the western boundary current was presumably involved, in conjunction with extreme weather. Based on recent works relying on the properties of Rossby waves at mid-latitudes, the present paper proposes a common cause for these intriguing phenomena.

4.2. Subtropical Cyclones

A low-pressure system is forming at the synoptic scale, the result of the merger of several low-pressure subsystems. To achieve this merger, dew-point fronts have to be formed, separating moist air masses found ahead of the dry line from drier air masses found behind it. The drier air behind dew-point fronts lifts up the moist air ahead, triggering

strong moist convection. A barometric trough gradually forms, which creates a convergence zone in the lower layers of the atmosphere and upper-level divergence.

The increasingly rapid rotation of cyclonic flows in the various atmospheric layers as they rise produces an extreme rainfall event. The rapid cycles of cyclogenesis contrast with the slowly maturing phenomena without which the cyclonic system could not have developed with such magnitude. They may lead to SST anomalies concomitant with the extreme rainfall event, which occur within the period bands centered on 1/12 and 1/24 yr. Monitoring these maturation processes could help predict the occurrence of devastating climatic phenomena.

The analysis of the different stages leading to subtropical low-pressure systems makes it possible to address an essential problem that relates to the presumed impact of anthropogenic forcing. One mechanism for the increase in such transient events discussed in the literature is related to the slowing of the predominant westerly wind circulation evident in observational data [66,67], due to a strong warming of the Arctic as a result of global warming [68]. Such a slowdown has been linked to observed increases in the persistence of weather systems [69,70].

By influencing the rapid cycles of cyclogenesis, such a mechanism could contribute to explaining the increase in the frequency of extreme rainfall events observed during the last decades in the northern hemisphere, in particular in the North America. But the ubiquity of the increase in the frequency as well as the intensity of extreme rainfall events also suggest an evolution in the mechanisms favoring the development of cyclonic flows at the synoptic scale. This hypothesis is corroborated by the fact that extreme rainfall events occur in places deemed not to be flood-prone, causing numerous victims, as happened in Germany in July 2021, thus deceiving the vigilance of weather-watch systems.

The development of coherent SST anomalies, the main driver of synoptic-scale subtropical cyclones, is unambiguously linked to the propagation of oceanic Rossby waves. These result from solar forcing, independent of anthropogenic forcing. In contrast, other mechanisms related to global warming appear to be decisive in the context of slow cycles during which the coalescence of low-pressure systems occurs. Such mechanisms are strengthened by a temperature increase of ocean surface water associated with an overall increase in atmospheric humidity, which lowers the dew point and favors the formation of fronts. In return, the extension of the low-pressure system at the synoptic scale centered on a continental low favors the feeding of the cyclonic flow by overlapping over surrounding SST anomalies. Owing to the accumulated latent heat, with regard to their internal energy these low-pressure systems promote upper-level lows, favoring blocks. This may explain the record precipitations observed during the last decades when pouring over regions deemed not to be flood prone, as has occurred in many places in Western and Central Europe.

5. Conclusions

The wavelet analysis of high temporal and spatial resolution data, namely SSH, geostrophic currents, and SST in the northwestern Pacific, allowed the highlighting of the formation of a mosaic of convergent and divergent cells along the north Pacific gyre from where the Kuroshio leaves the Asian continent to nearly 180°. Upwelling and downwelling are associated with Rossby waves of short apparent wavelengths embedded in the wind-driven current of the gyre. The driver of the fundamental Rossby wave and the harmonics is the declination of the sun. Sudden SSH anomalies may occur, some of them producing abrupt extensive positive or negative SST anomalies, opposite in sign to SSH anomalies from which they originated. This phenomenon is general and is observable along the subtropical gyres where the western boundary currents move away from the continents.

Regarding MHWs in the northwestern Pacific, a warm SST anomaly associated with the northward component of the wind resulting from the low-pression system induces an SST response to latent and sensible heat transfer where the latitudinal SST gradient is steep. The SST anomaly is then shifted north while the phases become uniform.

The wavelet analysis of high temporal and spatial resolution of SSH, SST, and rainfall height in the North Atlantic, the Baltic Sea, and northwest Europe has made it possible to highlight the evolution of an extratropical cyclone in northwestern Europe, of exceptional intensity, at different time scales. Intensification of subtropical cyclones as well as the increase in their frequency appear to be mainly related to the evolution of conditions favoring the formation of low-pressure systems at the synoptic scale. These conditions are probably exacerbated by anthropogenic warming which promotes the maturation of the mechanisms leading to the coalescence of lows. In these conditions, the interactions between the atmosphere and the coherent positive SST anomalies on the surrounding ocean play a major role in feeding the cyclonic flow centered on a continental low. Owing to the accumulated latent heat, extreme subtropical cyclones induce upper-level lows that favor the persistence of the cyclonic flow.

The innovative nature of this study is based on the dynamics of the various systems implicated in the formation of extreme climatic events. These events are the culmination of exceptional circumstances, some of which are foreseeable due to their relatively long maturation time. Some avenues are developed with the aim of better understanding how anthropogenic warming can modify certain key mechanisms in the evolution of the dynamic system at the interface between the oceans and the atmosphere.

Future work will focus on the role played by the anthropogenic forcing in the formation of extensive MHWs. On the other hand, by taking advantage of high-resolution data on geostrophic currents, a systematic study of short-period Rossby waves developing where the western boundary currents leave the continents to re-enter the subtropical gyres would be rich in teaching how to specify their climatic impacts, including the conditions of formation of MHWs and extreme rainfall events. Using the same method of investigation, other case studies focusing in particular on the southern hemisphere are required with the aim of generalizing these investigations.

Funding: This research received no external funding.

Data Availability Statement: Only public data duly referenced are used.

Conflicts of Interest: The author declares no conflict of interest.

References

1. Pinault, J.-L. A Review of the Role of the Oceanic Rossby Waves in Climate Variability. *J. Mar. Sci. Eng.* **2022**, *10*, 493. [CrossRef]
2. Yao, Y.; Wang, J.; Yin, J.; Zou, X. Marine heatwaves in China's marginal seas and adjacent offshore waters: Past, Present, and Future. *J. Geophys. Res. Oceans* **2020**, *125*, e2019JC015801. [CrossRef]
3. Li, Z.; Holbrook, N.J.; Zhang, X.; Oliver, E.C.J.; Cougnon, E.A. Remote Forcing of Tasman Sea Marine Heatwaves. *J. Clim.* **2020**, *33*, 5337–5354. [CrossRef]
4. Liu, K.; Xu, K.; Zhu, C.; Liu, B. Diversity of Marine Heatwaves in the South China Sea Regulated by ENSO Phase. *J. Clim.* **2022**, *35*, 877–893. [CrossRef]
5. Walsh, J.E.; Thoman, R.L.; Bhatt, U.S.; Bieniek, P.A.; Brettschneider, B.; Brubaker, M.; Danielson, S.; Lader, R.; Fetterer, F.; Holderied, K.; et al. The High Latitude Marine Heat Wave of 2016 and Its Impacts on Alaska. *Bull. Am. Meteorol. Soc.* **2018**, *99*, S39–S43. [CrossRef]
6. Chen, K.; Gawarkiewicz, G.; Yang, J. Mesoscale and Submesoscale Shelf-Ocean Exchanges Initialize an Advective Marine Heatwave. *J. Geophys. Res. Oceans* **2021**, *127*, e2021JC017927. [CrossRef]
7. Maggiorano, A.; Feng, M.; Wang, X.H.; Ritchie, L.; Stark, C.; Colberg, F.; Greenwood, J. Hydrodynamic drivers of the 2013 marine heatwave on the North West Shelf of Australia. *J. Geophys. Res. Oceans* **2021**, *126*, e2020JC016495. [CrossRef]
8. Benthuysen, J.A.; Oliver, E.C.J.; Feng, M.; Marshall, A.G. Extreme marine warming across tropical Australia during austral summer 2015–2016. *J. Geophys. Res. Oceans* **2018**, *123*, 1301–1326. [CrossRef]
9. Kuroda, H.; Taniuchi, Y.; Kasai, H.; Nakanowatari, T.; Setou, T. Co-occurrence of marine extremes induced by tropical storms and an ocean eddy in summer 2016: Anomalous hydrographic conditions in the Pacific shelf waters off southeast Hokkaido, Japan. *Atmosphere* **2021**, *12*, 888. [CrossRef]
10. Marin, M.; Bindoff, N.L.; Feng, M.; Phillips, H.E. Slower long-term coastal warming drives dampened trends in coastal marine heatwave exposure. *J. Geophys. Res. Oceans* **2021**, *126*, e2021JC017930. [CrossRef]
11. Marin, M.; Feng, M.; Phillips, H.E.; Bindoff, N.L. A global, multiproduct analysis of coastal marine heatwaves: Distribution, characteristics and long-term trends. *J. Geophys. Res. Oceans* **2021**, *126*, e2020JC016708. [CrossRef]

12. Feng, M.; Zhang, X.; Oke, P.; Monselesan, D.; Chamberlain, M.; Matear, R.; Schiller, A. Invigorating Ocean boundary current systems around Australia during 1979–2014: As simulated in a near-global eddy-resolving ocean model. *J. Geophys. Res. Oceans* **2016**, *121*, 3395–3408. [CrossRef]
13. Perkins-Kirkpatrick, S.E.; King, A.D.; Cougnon, E.A.; Holbrook, N.J.; Grose, M.R.; Oliver EC, J.; Lewis, S.C.; Pourasghar, F. The Role of Natural Variability and Anthropogenic Climate Change in the 2017/2018 Tasman Sea Marine Heatwave. *Bull. Am. Meteorol. Soc.* **2019**, *100*, S105–S110. [CrossRef]
14. Dosser, H.V.; Waterman, S.; Jackson, J.M.; Hannah, C.G.; Evans, W.; Hunt, B.P.V. Stark physical and biogeochemical differences and implications for ecosystem stressors in the Northeast Pacific coastal ocean. *J. Geophys. Res. Oceans* **2021**, *126*, e2020JC017033. [CrossRef]
15. Delgadillo-Hinojosa, F.; Félix-Bermúdez, A.; Torres-Delgado, E.V.; Durazo, R.; Camacho-Ibar, V.; Mejía, A.; Ruiz, M.C.; Linacre, L. Impacts of the 2014–2015 warm-water anomalies on nutrients, chlorophyll-a and hydrographic conditions in the coastal zone of northern Baja California. *J. Geophys. Res. Oceans* **2020**, *125*, e2020JC016473. [CrossRef]
16. Fumo, J.T.; Carter, M.L.; Flick, R.E.; Rasmussen, L.L.; Rudnick, D.L.; Iacobellis, S.F. Contextualizing marine heatwaves in the Southern California bight under anthropogenic climate change. *J. Geophys. Res. Oceans* **2020**, *125*, e2019JC015674. [CrossRef]
17. Miyama, T.; Minobe, S.; Goto, H. Marine heatwave of sea surface temperature of the Oyashio region in summer in 2010–2016. *Front. Mar. Sci.* **2021**, *7*, 576240. [CrossRef]
18. Yao, Y.; Wang, C. Variations in summer marine heatwaves in the South China Sea. *J. Geophys. Res. Oceans* **2021**, *126*, e2021JC017792. [CrossRef]
19. Gao, G.; Marin, M.; Feng, M.; Yin, B.; Yang, D.; Feng, X.; Ding, Y.; Song, D. Drivers of marine heatwaves in the East China Sea and the South Yellow Sea in three consecutive summers during 2016–2018. *J. Geophys. Res. Oceans* **2020**, *125*, e2020JC016518. [CrossRef]
20. Saranya, J.S.; Roxy, M.K.; Dasgupta, P.; Anand, A. Genesis and trends in marine heatwaves over the tropical Indian Ocean and their interaction with the Indian summer monsoon. *J. Geophys. Res. Oceans* **2020**, *127*, e2021JC017427. [CrossRef]
21. Kuroda, H.; Setou, T. Extensive Marine Heatwaves at the Sea Surface in the Northwestern Pacific Ocean in Summer 2021. *Remote Sens.* **2021**, *13*, 3989. [CrossRef]
22. Hayashi, M.; Shiogama, H.; Emori, S.; Ogura, T.; Hirota, N. The northwestern Pacific warming record in August 2020 occurred under anthropogenic forcing. *Geophys. Res. Lett.* **2021**, *48*, e2020GL090956. [CrossRef]
23. Myhre, G.; Alterskjær, K.; Stjern, C.W.; Hodnebrog, Ø.; Marelle, L.; Samset, B.H.; Sillmann, J.; Schaller, N.; Fischer, E.; Schulz, M.; et al. Frequency of extreme precipitation increases extensively with event rareness under global warming. *Sci. Rep.* **2019**, *9*, 16063. [CrossRef] [PubMed]
24. Sillmann, J.; Kharin, V.V.; Zwiers, F.W.; Zhang, X.; Bronaugh, D. Climate Extremes Indices in the CMIP5 Multimodel Ensemble. Part 2: Future Climate Projections. *J. Geophys. Res. Atmos.* **2013**, *118*, 2473–2493. [CrossRef]
25. Giorgi, F.; Coppola, E.; Raffaele, F. A Consistent Picture of the Hydroclimatic Response to Global Warming from Multiple Indices: Models and Observations. *J. Geophys. Res. Atmos.* **2014**, *119*, 11695–11708. [CrossRef]
26. Lehmann, J.; Coumou, D.; Frieler, K. Increased record-breaking precipitation events under global warming. *Clim. Chang.* **2015**, *132*, 501–515. [CrossRef]
27. Fischer, E.; Knutti, R. Detection of spatially aggregated changes in temperature and precipitation extremes. *Geophys. Res. Lett.* **2014**, *41*, 547–554. [CrossRef]
28. Dong, S.; Sun, Y.; Li, C.; Zhang, X.; Min, S.K.; Kim, Y.H. Attribution of extreme precipitation with updated observations and CMIP6 simulations. *J. Clim.* **2021**, *34*, 871–881. [CrossRef]
29. Sun, Q.; Zhang, X.; Zwiers, F.; Westra, S.; Alexander, L.V. A global, continental, and regional analysis of changes in extreme precipitation. *J. Clim.* **2021**, *34*, 243–258. [CrossRef]
30. Hawcroft, M.; Walsh, E.; Hodges, K.; Zappa, G. Significantly increased extreme precipitation expected in Europe and North America from subtropical cyclones. *Environ. Res. Lett.* **2018**, *13*, 124006. [CrossRef]
31. Pinault, J.-L. Regions Subject to Rainfall Oscillation in the 5–10 Year Band. *Climate* **2018**, *6*, 2. [CrossRef]
32. Pinault, J.-L. Global warming and rainfall oscillation in the 5–10 year band in Western Europe and Eastern North America. *Clim. Chang.* **2012**, *114*, 621–650. [CrossRef]
33. Easterling, D.R.; Arnold, J.R.; Knutson, T.; Kunkel, K.E.; LeGrande, A.N.; Leung, L.R.; Vose, R.S.; Waliser, D.E.; Wehner, M.F. Precipitation Change in the United States. In *Climate Science Special Report: Fourth National Climate Assessment, Volume I*; Wuebbles, D., Fahey, J.D.W., Hibbard, K.A., Eds.; U.S. Global Change Research Program: Washington, DC, USA, 2017.
34. Feng, Z.; Leung, L.R.; Hagos, S.; Houze, R.A.; Burleyson, C.D.; Balaguru, K. More frequent intense and long-lived storms dominate the springtime trend in central US rainfall. *Nat. Commun.* **2016**, *7*, 13429. [CrossRef] [PubMed]
35. Changnon, S.A.; Westcott, N.E. Heavy rainstorms in Chicago: Increasing frequency, altered impacts and future implications. *J. Am. Water Resour. Assoc.* **2002**, *38*, 1467–1475. [CrossRef]
36. *Managing the Risks of Extreme Events and Disasters to Advance Climate Change Adaptation. Special Report of the Intergovernmental Panel on Climate Change*; Cambridge University Press: Cambridge, UK, 2012. Available online: https://www.ipcc.ch/report/managing-the-risks-of-extreme-events-and-disasters-to-advance-climate-change-adaptation/ (accessed on 27 April 2022).
37. Rajczak, J.; Pall, P.; Schär, C. Projections of Extreme Precipitation Events in Regional Climate Simulations for Europe and the Alpine Region. *J. Geophys. Res. Atmos.* **2013**, *118*, 3610–3626. [CrossRef]

38. Rajczak, J.; Schär, C. Projects of Future Precipitation Extremes Over Europe: A Multimodel Assessment of Climate Simulations. *J. Geophys. Res. Atmos.* **2017**, *122*, 10773–10800. [CrossRef]
39. Zeder, J.; Fischer, E.M. Observed extreme precipitation trends and scaling in Central Europe. *Weather Clim. Extrem.* **2020**, *29*, 100266. [CrossRef]
40. Ali, H.; Fowler, H.J.; Lenderink, G.; Lewis, E.; Pritchard, D. Consistent Large-Scale Response of Hourly Extreme Precipitation to Temperature Variation Over Land. *Geophys. Res. Lett.* **2021**, *48*, e2020GL090317. [CrossRef]
41. Blöschl, G.; Hall, J.; Viglione, A.; Perdigão, R.A.; Parajka, J.; Merz, B.; Lun, D.; Arheimer, B.; Aronica, G.T.; Bilibashi, A. Changing climate both increases and decreases European river floods. *Nature* **2019**, *573*, 108–111. [CrossRef]
42. Blöschl, G.; Kiss, A.; Viglione, A.; Barriendos, M.; Böhm, O.; Brázdil, R.; Coeur, D.; Demarée, G.; Llasat, M.C.; Macdonald, N. Current European flood-rich period exceptional compared with past 500 years. *Nature* **2020**, *583*, 560–566. [CrossRef]
43. Willner, S.N.; Levermann, A.; Zhao, F.; Frieler, K. Adaptation required to preserve future high-end river flood risk at present levels. *Sci. Adv.* **2018**, *4*, eaao1914. [CrossRef] [PubMed]
44. Dottori, F.; Szewczyk, W.; Ciscar, J.C.; Zhao, F.; Alfieri, L.; Hirabayashi, Y.; Bianchi, A.; Mongelli, I.; Frieler, K.; Betts, R.A.; et al. Increased human and economic losses from river flooding with anthropogenic warming. *Nat. Clim. Chang.* **2018**, *8*, 781–786. [CrossRef]
45. Jacob, D.; Petersen, J.; Eggert, B.; Alias, A.; Christensen, O.B.; Bouwer, L.M.; Braun, A.; Colette, A.; Déqué, M.; Georgievski, G.; et al. EURO-CORDEX: New High-Resolution Climate Change Projections for European Impact Research. *Reg. Environ. Chang.* **2014**, *14*, 563–578. [CrossRef]
46. Chakravorty, S.; Gnanaseelan, C.; Chowdary, J.S.; Luo, J.-J. Relative role of El Niño and IOD forcing on the southern tropical Indian Oceanic Rossby waves. *J. Geophys. Res. Oceans* **2014**, *119*, 8. [CrossRef]
47. Sprintall, J.; Cravatte, S.; Dewitte, B.; Du, Y.; Gupta, A.S. ENSO Oceanic Teleconnections. In *El Niño Southern Oscillation in a Changing Climate*; McPhaden, M.J., Santoso, A., Cai, W., Eds.; American Geophysical Union: Washington, DC, USA, 2020. [CrossRef]
48. Webber, B.G.; Matthews, A.J.; Heywood, K.J.; Kaiser, J.; Schmidtko, S. Seaglider observations of equatorial Indian Oceanic Rossby waves associated with the Madden-Julian Oscillation. *J. Geophys. Res. Oceans* **2014**, *119*, 6. [CrossRef]
49. Gill, A.E. *Atmosphere-Ocean Dynamics, International Geophysics Series 30*; Academic Press: Cambridge, MA, USA, 1982; 662p.
50. Pinault, J.-L. Resonantly Forced Baroclinic Waves in the Oceans: Subharmonic Modes. *J. Mar. Sci. Eng.* **2018**, *6*, 78. [CrossRef]
51. Pinault, J.-L. Resonantly Forced Baroclinic Waves in the Oceans: A New Approach to Climate Variability. *J. Mar. Sci. Eng.* **2021**, *9*, 13. [CrossRef]
52. Choi, M.Y.; Thouless, D.J. Topological interpretation of subharmonic mode locking in coupled oscillators with inertia. *Phys. Rev. B* **2001**, *64*, 014305. [CrossRef]
53. Sea Level Anomaly and Geostrophic Currents, Multi-Mission, Global, Optimal Interpolation, Gridded, Are Provided by the National Oceanic and Atmospheric Administration (NOAA). Available online: https://coastwatch.noaa.gov/pub/socd/lsa/rads/sla/daily/nrt/ (accessed on 19 November 2021).
54. Daily Sea Surface Temperature Is Provided by NOAA. Available online: https://www.ncei.noaa.gov/data/sea-surface-temperature-optimum-interpolation/v2.1/access/avhrr/ (accessed on 8 January 2022).
55. Reynolds, R.W.; Smith, T.M.; Liu, C.; Chelton, D.B.; Casey, K.S.; Schlax, M.G. Daily High-Resolution-Blended Analyses for Sea Surface Temperature. *J. Clim.* **2007**, *20*, 5473–5496. [CrossRef]
56. Banzon, V.; Smith, T.M.; Chin, T.M.; Liu, C.; Hankins, W. A long-term record of blended satellite and in situ sea-surface temperature for climate monitoring, modeling and environmental studies. *Earth Syst. Sci. Data* **2016**, *8*, 165–176. [CrossRef]
57. Huang, B.; Liu, C.; Banzon, V.; Freeman, E.; Graham, G.; Hankins, B.; Smith, T.; Zhang, H.M. Improvements of the Daily Optimum Interpolation Sea Surface Temperature (DOISST) Version v2.1. *J. Clim.* **2021**, *34*, 2923–2939. [CrossRef]
58. Global Daily Precipitation Is Provided by NOAA. Available online: https://www.ncei.noaa.gov/data/global-precipitation-climatology-project-gpcp-daily/access/ (accessed on 25 March 2022).
59. Report of Global Precipitation Climatology Project (GPCP). Available online: https://www.ncei.noaa.gov/data/global-precipitation-climatology-project-gpcp-daily/doc/CDRP-ATBD-0913%20Rev%200%20Precipitation%20-%20GPCP%20Daily%20C-ATBD%20(01B-35)%20(DSR-1159).pdf (accessed on 25 March 2022).
60. Huffman, G.J.; Adler, R.F.; Morrissey, M.M.; Bolvin, D.T.; Curtis, S.; Joyce, R.; McGavock, B.; Susskind, J. Global Precipitation at One-Degree Daily Resolution from Multisatellite Observations. *J. Hydrometeorol.* **2001**, *2*, 36–50. [CrossRef]
61. Torrence, C.; Compo, G.P. A Practical Guide to Wavelet Analysis. *Bull. Am. Meteorol. Soc.* **1998**, *79*, 61–78. [CrossRef]
62. Pinault, J.-L.; Pereira, L. What Speleothems Tell Us about Long-Term Rainfall Oscillation throughout the Holocene on a Planetary Scale. *J. Mar. Sci. Eng.* **2021**, *9*, 853. [CrossRef]
63. The Watchers. Available online: https://watchers.news/2021/07/28/record-breaking-heatwave-hokkaido-japan-july-2021/ (accessed on 7 January 2021).
64. Wash, C.H.; Heikkinen, S.H.; Liou, C.S.; Nuss, W.A. A Rapid Cyclogenesis Event during GALE IOP 9. *Mon. Weather Rev.* **1990**, *118*, 234–257. [CrossRef]
65. Wallace, J.M.; Hobbs, P.V. *Atmospheric Science: An Introductory Survey*; University of Washington: Seattle, WA, USA, 2006.
66. The July 2021 Floods in Germany and the Climate Crisis—A Statement by Members of Scientists for Future. Available online: https://info-de.scientists4future.org/the-july-2021-floods-in-germany-and-the-climate-crisis/ (accessed on 22 January 2022).

67. Coumou, D.; Lehmann, J.; Beckmann, J. The weakening summer circulation in the Northern Hemisphere mid-latitudes. *Science* **2015**, *348*, 324–327. [CrossRef] [PubMed]
68. Kornhuber, K.; Tamarin-Brodsky, T. Future Changes in Northern Hemisphere Summer Weather Persistence Linked to Projected Arctic Warming. *Geophys. Res. Lett.* **2021**, *48*, e2020GL091603. [CrossRef]
69. Pfleiderer, P.; Coumou, D. Quantification of temperature persistence over the Northern Hemisphere land-area. *Clim. Dyn.* **2018**, *51*, 627–637. [CrossRef]
70. Harvey, B.J.; Cook, P.; Shaffrey, L.C.; Schiemann, R. The Response of the Northern Hemisphere Storm Tracks and Jet Streams to Climate Change in the CMIP3, CMIP5, and CMIP6 Climate Models. *J. Geophys. Res. Atmos.* **2020**, *125*, e2020JD032701. [CrossRef]